RESEARCH ARTICLE

Experimental investigation of the wall shear stress and the vortex dynamics in a circular impinging jet

**Mouhammad El Hassan · Hassan Hassan Assoum ·
Vaclav Sobolik · Jérôme Vétel · Kamel Abed-Meraim ·
André Garon · Anas Sakout**

Abstract The wall shear stress and the vortex dynamics in a circular impinging jet are investigated experimentally for Re = 1,260 and 2,450. The wall shear stress is obtained at different radial locations from the stagnation point using the polarographic method. The velocity field is given from the time resolved particle image velocimetry (TR-PIV) technique in both the free jet region and near the wall in the impinging region. The distribution of the momentum thickness is also inspected from the jet exit toward the impinged wall. It is found that the wall shear stress is correlated with the large-scale vortex passing. Both the primary vortices and the secondary structures strongly affect the variation of the wall shear stress. The maximum mean wall shear stress is obtained just upstream from the secondary vortex generation where the primary structures impinge the wall. Spectral analysis and cross-correlations between the wall shear stress fluctuations show that the vortex passing influences the wall shear stress at different locations simultaneously. Analysis of cross-correlations between temporal fluctuations of the wall shear stress and the transverse vorticity brings out the role of different vortical structures on the wall shear stress distribution for the two Reynolds numbers.

1 Introduction

Impinging jets have been widely studied during the last 5 decades because of their multiple industrial applications.

M. El Hassan (✉) · J. Vétel · A. Garon
Department of Mechanical Engineering, LADYF,
École Polytechnique de Montréal, C.P. 6079,
Succursale Centre-ville, Montréal, Québec H3C 3A7, Canada
e-mail: elhassanmoh@yahoo.fr

H. H. Assoum · V. Sobolik · K. Abed-Meraim · A. Sakout
LaSIE, Université de La Rochelle, La Rochelle, France

Several studies have been conducted on the physics of the impinging jet flow in order to understand the influence of different flow parameters, such as the Reynolds number, the wall to the jet exit distance and the jet nozzle geometry on the mass and heat transfer rates. Most of the previous studies dealt with heat transfer as discussed in the review papers of Martin (1977), Downs and James (1987), Hrycak (1981), Jambunathan et al. (1992) and Lee and Lee (2000). It should be mentioned that few studies quantified experimentally the wall shear stress at the impinged wall. The impinging jets can be used to extract particles from surfaces or as a method of cleaning or taking samples for chemical analysis, for example, for the detection of explosives (Phares et al. 2000a).

Theoretically, two approaches were proposed to solve the problem of the impinging jet: the first approach consists in solving the Navier-Stokes equations considering the jet as one region (Deshpande and Vaishnav 1982; Looney and Walsh 1984; Bouainouche et al. 1997). The second approach divides the jet into separate regions (suggested by Bradshaw and Love 1961); different approximations for the Navier Stokes equations are taken for each zone (Strand 1964; Scholtz and Trass 1970; Rubel 1980, 1983). Generally, an impinging jet has been separated into three distinct zones of evolution: the free jet, the stagnation zone and the radial wall-jet region, and each one is characterized by its proper flow dynamics. The zone of interaction between the vortices and the wall was described by Walker et al. (1987) in an experimental study and Orlandi and Verzicco (1993) in a numerical simulation. The impinging jets are generally dominated by vortices, which interact with the impinged wall and are responsible for surface pressure fluctuations and variations of the wall shear stress. Therefore, the understanding of the vortex dynamics in different regions of the impinging jet is of high interest

fundamentally and for practical purposes. Some studies have investigated the flow field associated with the collision of the jet on a flat surface. Among the most notable, we can mention Cerra and Smith (1983), Orlandi and Verzicco (1993) and Fabris et al. (1996). Ho and Nosseir (1981) revealed a feedback phenomenon, which can control the jet at the nozzle exit for high-speed subsonic impinging jets. Naguib and Koochesfahani (2004) investigated the physics of the wall-pressure generation process as well as the nature of the wall-pressure flow sources associated with the vortex ring/wall interaction. They found that in the vortex-wall interaction, positive pressure is produced by intensification of the field of strain rate by the vortex near the wall and generates a region of high strain rate due to the separation of the boundary layer under the influence of the incident primary vortex. Poreh et al. (1967) considered an impinging circular jet on a flat plate. They found that the velocity decreases with distance from the stagnation point and that the turbulence intensities were higher near the wall than the other regions. However, no correlation was observed between the turbulent shear stress and the local gradient of the mean velocities. Yokobori et al. (1983) considered the plane impinging jet and detected counter-rotating vortex pairs along the wall. Sakakibara et al. (1997, 2001) also observed that the counter-rotating vortex pairs are convected from an upstream location and stretched in the vicinity of the wall. Nishino et al. (1997) performed measurements using the particle-tracking velocimetry technique on an impinging jet flow. Their investigation showed that the radial velocity magnitude increases highly as the impinged wall is approached. The axial turbulent intensity first grows toward the wall with the development of the jet, and then, it decreases sharply near the wall after a peak at $Y/D = 0.25$. The radial turbulent intensity rises near the wall and exceeds the axial one for $Y/D < 0.1$. The turbulent kinetic energy exhibits an increase similar to that of the radial component near the wall. Kataoka and Mizushina (1974), Alekseenko et al. (1997, 2002) and Vejrazka et al. (2005) studied the effect of the instabilities in the shear layer of the impinging jet on the flow structure and transfer rates. Hadziabdic and Hanjalic (2008) performed a large-eddy simulation on a circular impinging jet in order to better understand the vortex dynamics. They found that the dominant event that governs the flow is the roll-up of vortices, which appear in the shear layer and then travel downstream; the large-scale structures hitting the wall are neither circular nor parallel to the wall, but angled and fragmented into segments. The radial flow propagation leads to vortex stretching in the azimuthal direction that enhances their rotation. Consequently, counter-rotating vortices are formed very close to the wall. These vortices attached to the wall, taking place as recirculation bubbles

are further stretched before they are destroyed, and driven into the turbulent wall-jet. The presence of these vortices increases the level of turbulence in this region. Harvey and Perry (1971) were the first who observed the process of wall separation and the generation of secondary vortex downstream of the associated primary vortex. Later, flow visualization studies corroborated these findings in vortex ring impinging flow (e.g., Popiel and Trass 1991; Liang et al. 1983; Cerra and Smith 1983). Doligalski (1994) stated that in general the turbulent horseshoe vortex induces the generation of secondary vortices. These vortices grow and are ejected from the surface in a strong, narrow-band eruption of surface fluid. Janetzke and Nitsche (2009) investigated the effects of jet pulsation on flow field and wall shear stress of an impingement jet. They found that the occurrence of secondary vortices at the wall is induced by the impinging primary vortices. They also observed that the boundary layer at the wall is periodically disrupted and regenerated, which results in very high transient wall shear stress due to the high vortex strength. Among the studies that investigated the wall shear stress, Zhe and Modi (2001) estimated the mean wall shear stress on the impingement surface using hot-wire anemometry measurements. They found that the skin friction at the target surface depends upon the distance of the target surface from the slot. However, the variation among the three nozzle-to-wall distances investigated (2, 3 and 4 jet diameters) was found to be small. They also evidenced that the skin friction coefficient is Reynolds number independent for Reynolds numbers between 10,000 and 20,000. Loureiro and Freire (2009) used two different ways to quantify the wall shear stress using a Micro-sensor (an optical MEMS-based velocity gradient sensor) from Measurement Science Enterprise Inc. (Fourguette et al. 2001; Gharib et al. 2002) and the slope of the velocity distribution in the logarithmic sublayer (Clauser 1956). Smedley et al. (1999) described an experimental study of the removal of fine (8.3 μm) polystyrene particles from a glass substrate using a gas impinging jet. Results suggest that the particles act as nearly quantized shear stress sensors that provide a direct, though as yet uncalibrated, measure of the surface shear stress. Yapici et al. (1999) measured the surface local mean shear stress for a round submerged jet, with a fully developed turbulent velocity profile, impinging on a flat surface, using the electrochemical technique for Reynolds numbers ranging from 9,200 to 73,500, and nozzle-to-plate distances from 2 to 10 jet diameters. Their results showed that the non-dimensional local shear stress values decrease with increasing Reynolds number and becomes almost constant at higher Reynolds numbers. They also found that the highest peak in the radial distribution of the wall shear stress was obtained for the dimensionless nozzle to impingement surface of 4 and the height of the peak

reduced with increasing H/D. Although the wall shear stress was obtained experimentally using different techniques, many difficulties were encountered by authors regarding an accurate measurement. Despite the invested efforts in laser methods, the errors persist and the various techniques remain under development. In addition, the measurements taken using the Preston tube may induce many errors. Phares et al. (2000b) compared several data of wall shear stress measurements found in the literature with theoretical predictions. They found that the Preston tube induces errors, particularly when the logarithmic region of the boundary layer is not well defined. They also stated that the electrochemical method is the most precise of any indirect method for the impingement-region wall shear stress measurements. To our knowledge, there is no experimental study that associates both PIV and electrochemical techniques to investigate the parietal wall shear coupled with the vortices field of an axisymmetric jet. The present work is an experimental investigation focusing on the relation between the vortex dynamics in different regions of a circular impinging jet and the wall shear stress at the impinged wall. PIV measurements associated with the velocity gradient at the wall using electrodiffusion probes are presented. Results are shown and discussed for two Reynolds numbers.

2 Experimental apparatus and procedures

2.1 Jet flow facility

Figure 1 shows the experimental device designed to allow simultaneous measurements of 2D velocity field and wall shear rate in an impinging jet using the PIV and the polarographic method, respectively. A gear pump draws its supply from the reservoir and delivers the electrolyte to the nozzle. The fluid impinges the circular target disk equipped with electrodes. The temperature of the fluid is controlled by the cooling coil within ± 0.2°C. The nozzle is screwed to a 200-mm length stainless steel tube with the inner and outer diameters of 15 and 20 mm, respectively. A honeycomb manufactured of 7-mm-thick disk by drilling 17 holes with a diameter of 2 mm was fitted in the tube inlet. The nozzle assembly is located in a support, which allowed vertical movement for accurate alignment of the nozzle axis with the target disk center. The reservoir is placed on the sliding compound table (Proxxon KT 150), which permitted movement in the direction along of and perpendicular to the tube axis with a precision of 0.05 mm. A transparent plate was used in the region where the laser penetrates the electrochemical solution to avoid the fluctuating surface waves. The entire piping system was made using inert component to electrochemical solution.

The target is manufactured of a Plexiglas disk with diameter 100 mm and thickness 17 mm by first drilling the holes to accommodate the electrodes. Then, a platinum foil with a diameter of 50 mm and thickness 50 μm was assembled centrally with Plexiglas disk using Neoprene glue. Holes with a diameter 0.7 mm were drilled through the platinum foil as the continuation of the holes in the Plexiglas disk. The electrodes were fabricated of a 0.5-mm platinum wire, which was coated electrophoretically with a deposit of a polymeric paint. After soldering connecting cables, the electrodes were glued with an epoxy resin into the Plexiglas disk, so that the tops of the platinum wires just projected above the platinum foil. The wires were then rubbed down flush with the surface of the platinum foil using progressively finer grades of emery paper. The last emery paper had a grit size 10 μm. The whole surface was then polished. The platinum wires were used for the measurements of wall shear rate and the platinum foil as anode. The electrode positions in the target disk are shown in Fig. 2.

The test fluid is a 20 mol/m^3 equimolar aqueous solution of potassium ferri/ferrocyanide with 1.5% K_2SO_4 by weight as supporting electrolyte. The density of the solution was 1,007 kg/m^3, kinematic viscosity 1.065×10^{-6}
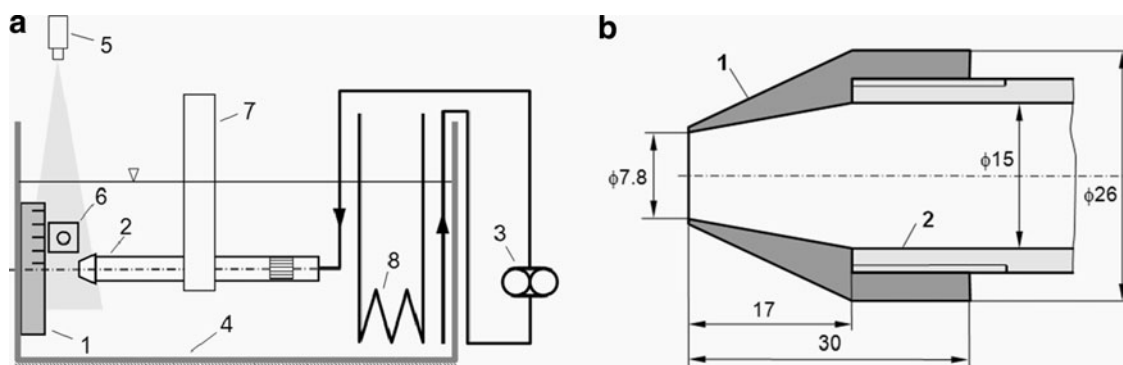

Fig. 1 **a** Jet facility sketch: (*1*) circular target disk; (*2*) cylindrical tube; (*3*) pump; (*4*) reservoir; (*5*) laser source; (*6*) high-speed camera; (*7*) support; (*8*) cooling coil. **b** Jet exit geometry: (*1*) circular nozzle; (*2*) upstream tube
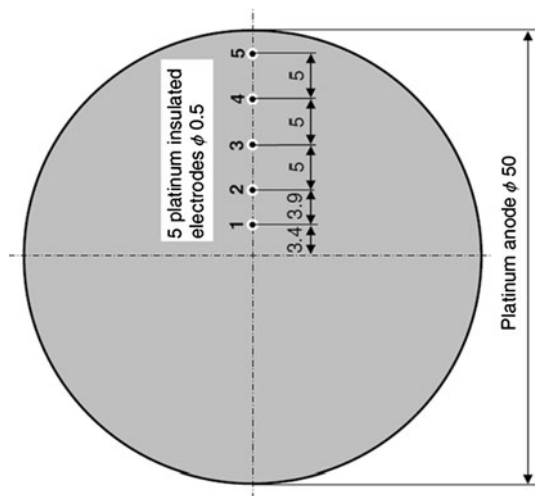
Fig. 2 Position of the polarographic probes on the impinged wall (dimensions are in mm)

m^2/s and diffusivity 7.5×10^{-10} m^2/s at 20°C. The resulting Schmidt number was 1,333. The used convergent nozzle had an outlet diameter of 7.8 mm with an area contraction 4:1 on a length of 17 mm. The distance from the impinged surface to the exit of the convergent is denote L. We can define a dimensionless distance L/D, which characterizes the distance from the disk, where D is the diameter of the nozzle at the exit. In this paper, $L/D = 2.08$ for all measurements. The studied Reynolds numbers, based on the diameter of the jet (D) and the exit velocity, are $Re = 1,260$ and $Re = 2,450$.

2.2 Time-resolved particle image velocimetry measurements

The time-resolved PIV system used for this study is composed of one Phantom V9 camera of $1,200 \times 1,632$ pixels^2, and a Nd : YLF NewWave Pegasus laser of 10 mJ energy and 527 nm wavelength, the laser sheet obtained by a system of lenses has a minimal thickness of 0.5 mm in the measurement section. The acquisition frequency of the PIV system is 500 Hz for a maximal image window. A number of 500 image pairs were acquired. Small glass spheres, 9 to 13 μm in diameter, are used as tracer for the PIV measurements. The camera is mounted on a traversing system in the normal direction of the light sheet plane of the laser. The synchronization between the laser and the camera is controlled by a LaVision High-Speed Controller, and the data acquisition is performed with DaVis 7.4 software, a CCD image acquisition and processing algorithm developed by LaVision. The time delay between two images in an image pair is 600 and 400 μs for $Re = 1,260$ and 2,450, respectively. The calculation of the two velocity components was obtained using a cross-correlation

between two views of the calibration target. The calibrated images provide a spatial resolution of 33.1 μm per pixel corresponding to a 52×38 mm^2 field of view. The images are processed by an adaptive multigrid algorithm correlation handling the distortion window and the subpixel window displacement. The prediction-correction method is validated for each size of the grid when the signal-to-noise ratio of the correlation is above a threshold of 1.1. On average, less than 2% of the vectors are detected as incorrect. These vectors are corrected by using a bilinear interpolation scheme. The final grid is composed of 32×32 pixels size interrogation windows with 50% overlap leading to a vector spacing of 13.5 pixels, which represents a spatial resolution of 0.65 mm. Holes are completed using a bilinear interpolation.

The average size of the particle image is 3×3 pixels, which is adequately resolved according to Prasad et al. (1992) with the absence of the peak locking phenomenon (Westerweel 1993). The accumulation of the rms error and the bias error gives a total error of about 3.7% of the mean axial velocity. The theoretical analysis of Westerweel (1993) is used to estimate the error on the particle image displacement. The maximal displacement error is equal to 1.5 and 2.3% for the longitudinal and the vertical velocity components.

2.3 The polarographic method

The polarographic (electrodiffusion) method is based on the measurement of limiting diffusion current on a working electrode (probe). For the total current I_L through a circular electrode in a viscosimetric flow with parallel streamlines and uniform wall shear rate γ, the formula corresponding to the Leveque's equivalent formula for heat transfer was established by Reiss and Hanratty (1962)

$$I_L = \frac{0.884\pi}{3^{1/3}\Gamma(4/3)} nFc\gamma^{1/3}D^{2/3}R^{5/3} \tag{1}$$

where Γ is the gamma function, n the number of electrons involved in the electrochemical reaction ($n = 1$ for the potassium ferro- and ferricyanide system), F the Faraday constant, c the bulk concentration, D the diffusivity of the active ions and R the radius of the electrode.

In the case of an impinging circular jet, the streamlines in the wall vicinity spread radially from the stagnation point. Due to the velocity component normal to the wall, the wall shear rate is not uniform and Eq. 1 does not hold exactly. This velocity component and its effect diminish with increasing distance from the stagnation point. Kristiawan et al. (2012) have shown that using Eq. 1 for an electrode with $R = 0.25$ mm at a distance $x = 1$ mm causes 2.1% error in wall shear rate. Taking this error as acceptable limiting value, we shall use Eq. 1 for the wall shear rate calculations at $x > 1$ mm.

The above given method, Eq. 1, can be used for the wall shear rate calculation from the measured limiting diffusion currents for steady and quasi-steady flows. If the flow is not steady, the inertia of diffusion boundary layer on the working electrode manifests itself as a filter, which diminishes amplitude and causes phase shift of the measured current. A simple method based on the integral balance for the calculation of the corrected values γ_{corr} was proposed by Sobolik et al. (1987):

$$\gamma_{corr} = \gamma \left[1 + 0.45 D^{-1/3} R^{2/3} \gamma^{-5/3} \frac{d\gamma}{dt} \right] \qquad (2)$$

where γ is the wall shear rate calculated from measured currents using the Eq. 1 (Rehimi et al. 2006) verified this method by numerical simulations.

The wall shear stress is calculated from wall shear rate using the Newton law:

$$\tau = \mu \gamma_{corr} \qquad (3)$$

where the dynamic viscosity had a value of 1.07×10^{-3} Pa s.

3 Results

3.1 The initial conditions

It is known that the development of the jet is strongly dependent on the initial conditions such as the jet geometry and the exit velocity and turbulence intensity distributions. The mean streamwise velocity and the mean longitudinal turbulence intensity profiles near the jet exit (at $Y/D = 0.1$) are given in the Fig. 3.

The coordinate origin is taken at the nozzle exit and the y-axis is along the axis of the pipe. U_x and U_y are the mean velocity components along the x-axis and the y-axis, respectively. u'_{rms} and v'_{rms} (respectively u' and v') are the velocity root-mean-squares (respectively, the velocity fluctuating components) in the x and the y directions. In the free jet region, the streamwise direction is considered along the y-axis.

Figure 3a shows that the velocity profile in the jet core region is flat for both the Reynolds numbers; the velocity drops to almost zero at X greater than the edge of the jet. The turbulence intensity (Fig. 3b) presents a flat distribution in the region of the jet core with value around 2% of the maximum outlet velocity. In the shear region, v'_{rms} presents a peak, which corresponds to the inflexion location in the velocity profile. The peaks amplitude is around 6% of the maximum outlet velocity for $Re = 1,260$ and around 8% for $Re = 2,450$. Similar turbulence intensity distribution was found by El Hassan and Meslem (2010) near the exit of a circular orifice jet for a Reynolds number of 3,600. A conical convergent geometry, similar to that of the present study, was used by the authors. However, the maximum turbulence intensity of their circular jet was around 6%, which is lower than the present value when the Reynolds number is considered. This difference can be attributed to the influence of the jet exit and the nozzle geometries on the turbulence intensity distribution. Consequently, the exit velocity profile of El Hassan et al. study was saddle-backed with a vena contracta effect near the circular jet edges.

3.2 Downstream evolution of the K-H instability upstream from the impinged wall

The jet dynamics is characterized by the amplification of the primary instability, formed at the exit, when traveling downstream along the jet axis. The roll-up of the shear layer
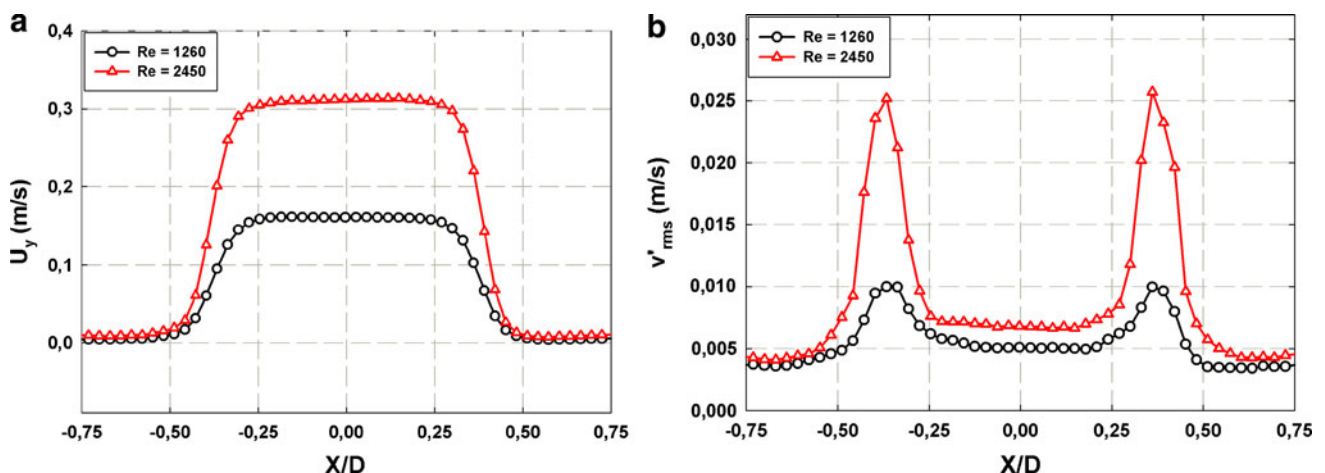

Fig. 3 Mean streamwise velocity (**a**) and longitudinal root-mean-square velocity (**b**) distributions near the jet exit (at 0.1 D) for $Re = 1,260$ and 2,450

is responsible for the generation of azimuthal large-scale structures, called Kelvin-Helmholtz (K-H) vortices. The downstream evolution of the momentum thickness is given to characterize the expansion of the free jet region in the longitudinal direction. The momentum thickness is calculated from the mean streamwise velocity profiles as follows

$$\theta = \int\limits_0^{x_{U_{min}}} \frac{U_y}{U_{0y}}\left(1 - \frac{U_y}{U_{0y}}\right)dx \qquad (4)$$

Where $x_{U_{min}}$ corresponds to the edge of the jet and U_{0y} is the maximum streamwise velocity at the studied longitudinal location. The edge of the jet is defined using the criterion proposed by El Hassan et al. (2011). Using this criterion, the minimum velocity is taken equal to 1.5% of the maximum mean streamwise velocity at the jet exit.

The momentum thickness calculation is only valid in the free jet region, upstream from the location where the flow turns from the wall normal to wall parallel and when most of the momentum is diverted to the radial direction due to the wall.

Figure 4 shows the downstream evolution of the momentum thickness in the free jet region and in the upstream part of the impinging region. The initial momentum thickness θ_0, calculated at $Y/D = 0.1$, is 0.47 and 0.925 for $Re = 1,260$ and 2,450, respectively. It is seen in the Fig. 4 that the momentum thickness increases downstream from the jet exit with an expansion rate higher for the lower Reynolds number. The expansion rate shows a decrease from $Y/D = 1.1$ for both the plots (Fig. 4). The momentum thickness reaches its maximum value at $Y/D = 1.2$ then θ becomes almost constant for Y/D between 1.2 and 1.35. The maximum value of the momentum thickness is equal to 0.51 for $Re = 1260$ and to 1 for $Re = 2450$. The presence of the impinged wall is responsible for the decrease in both the expansion rate and the momentum thickne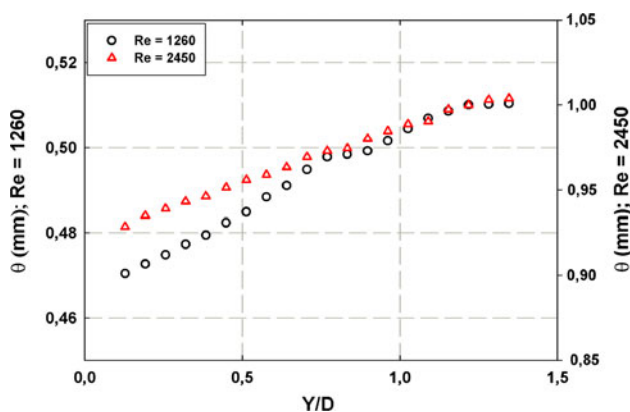ss when the wall is approached. The presence of the impinged wall is responsible for the decrease in both the expansion rate and the momentum thickness when the wall is approached.

Fig. 4 Longitudinal distribution of the momentum thickness

3.3 Mean streamwise velocity, turbulence intensity and skin friction coefficient distributions

The distribution of the mean longitudinal turbulence intensity is shown with the iso-values of the mean x-component of the velocity (U_x) in the Figs. 5 and 6 for $Re = 1,260$ and 2,450, respectively. The location of different polarographic probes (P1–P5) is shown in the same figures. Both the skin friction coefficient amplitude measured by the electrochemical probes and the corresponding root-mean-square are also given. It is seen that the zones where the azimuthal vortices develop are characterized by high turbulence intensity values. Indeed, when traveling from the jet exit toward the impinging wall, the turbulence intensity increases in the shear regions. Figure 5 shows that the velocity U_x has a peak between the probe P1 and P2, at around 1.5 mm from the wall ($Y = 14.5$ cm). It can be observed that the absolute value of U_x reaches a maximum between P1 and P2 and then decreases in the radial direction with a separation shape of the iso-velocity contours from the wall between P2 and P3. The highest values of the turbulence intensity in the wall region correspond to the impact region of the transverse structures. As the radial distance increases, the turbulence intensity decreases near the wall particularly downstream from the separation of the boundary layer, upstream from P3. When the Reynolds number increases (Fig. 6), the velocity and the turbulence intensity peaks remain between P1 and P2.

Figures 5 and 6 also show a decay in the wall shear stress when the radial distance increases, from the probe P1–P5; the maximum skin friction coefficient amplitude is reached at P1 for the two regimes ($C_f = 0.063$ and 0.039 for $Re = 1,260$ and 2,450, respectively). The exact position of the maximum skin friction coefficient value can be located between the probes P1 and P2. Additional polarographic measurements were taken for a better localization of the maximum wall shear stress and that of its fluctuations. It is interesting to note (Figs. 5 and 6) that the wall shear stress fluctuations are higher at the probe P2, while the mean skin friction coefficient is lower at this probe as compared to the probe P1. This behavior is related to the dynamics of the separated flow and the impact of the K-H vortical structures near the probe P2. Indeed, the impact of the transverse structures on the wall results in high local shear stress values, whereas the shear stress fluctuations increase as the vortices interact with the wall resulting in the birth of secondary vortices. This phenomenon seems to be more pronounced when increasing the Reynolds number.

3.4 Mean wall shear stress distribution and vortex dynamics

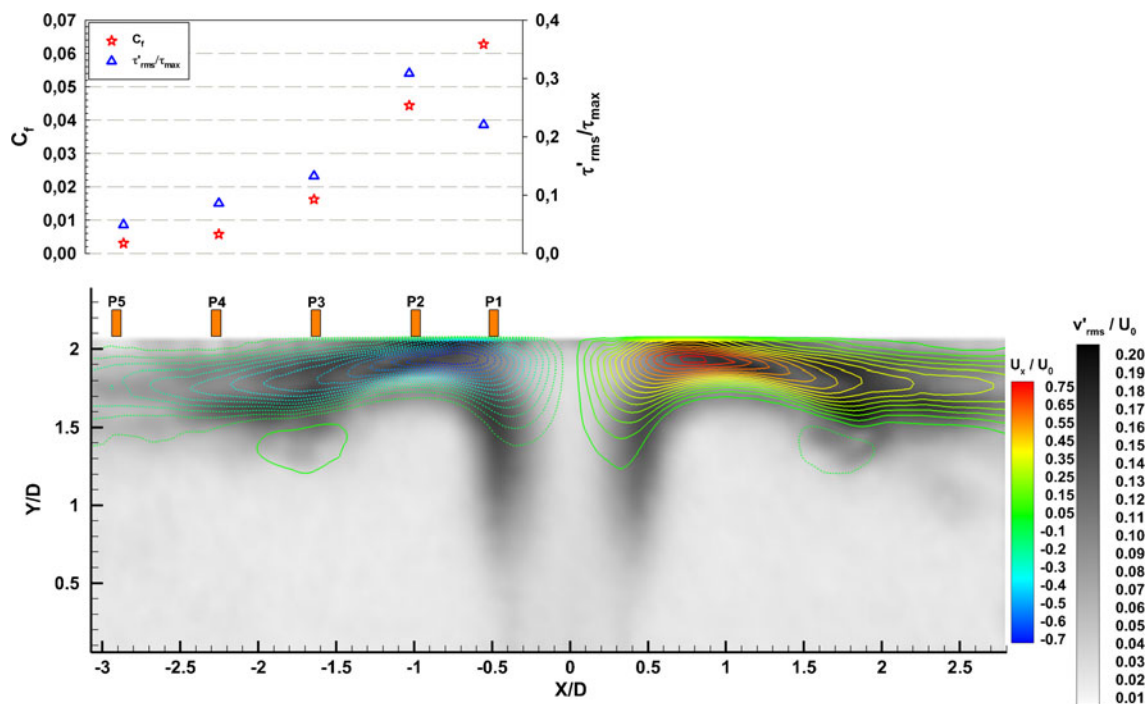More details about the variation of the shear stress at the impinged wall were obtained by moving the impinged

Fig. 5 Mean streamwise velocity (*contour lines*) and the longitudinal rms distributions; *top figure*: mean and rms wall shear stress; *Re* = 1,260
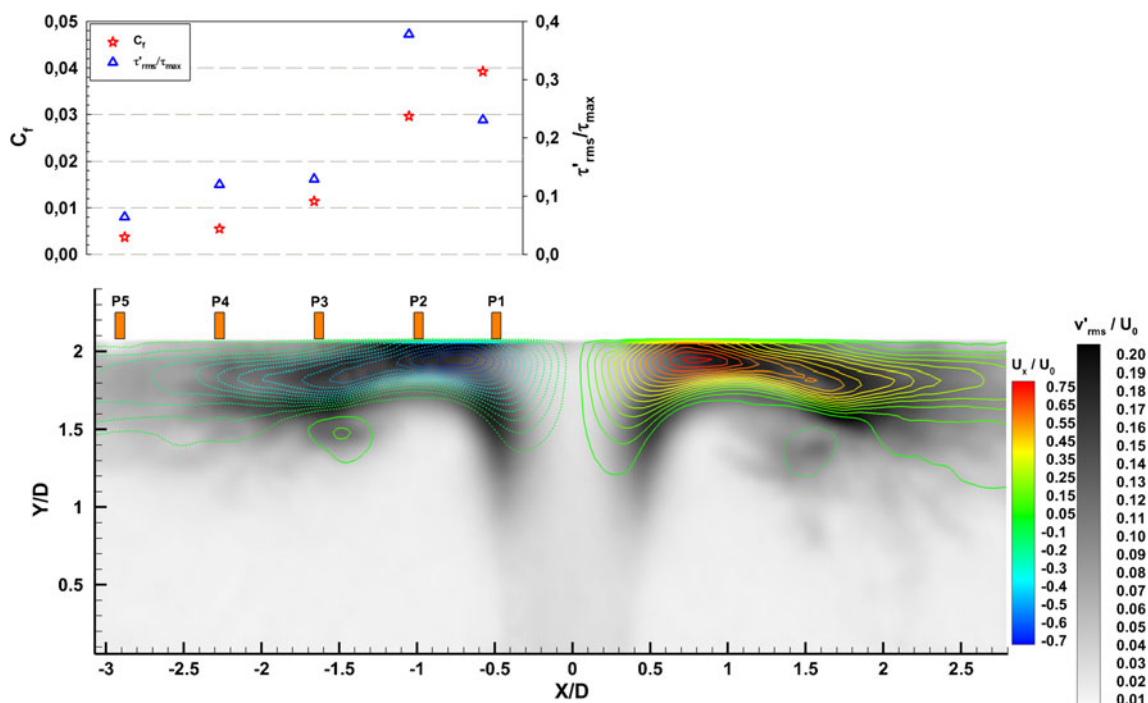

Fig. 6 Mean streamwise velocity (*contour lines*) and the longitudinal rms distributions; *top figure*: mean skin friction coefficient and rms of the wall shear stress; *Re* = 2,450

target in the radial direction. Figure 7 shows the distribution of the mean skin friction coefficient for *Re* = 1,260 and 2,450. The skin friction coefficient values obtained simultaneously with the PIV measurements are shown in the

same figure for comparison and as indication of the polarographic probe positions. It is clear that the average skin friction coefficient presents a symmetrical distribution. The maximum mean skin friction coefficient, equal to 0.07
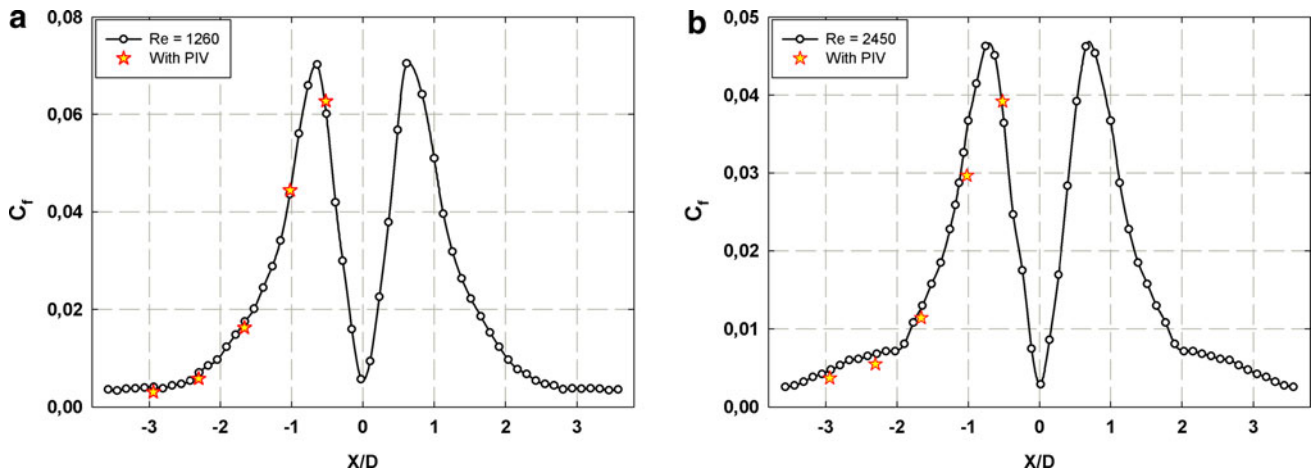
Fig. 7 Mean skin friction coefficient distribution at the impinged wall for $Re = 1,260$ and 2,450, respectively

and 0.046, is located between the probes P1 and P2 at around $0.64D$ and $0.72D$ for $Re = 1,260$ and 2,450, respectively. At the stagnation point, the skin friction coefficient is very low for the two studied Reynolds numbers. The vortex dynamics near the impinged wall is investigated for a better understanding of the skin friction coefficient variations at the wall. Four phases of the flow are shown in Figs. 8 and 9 for both Reynolds numbers; the time delay between two consecutive phases is 10 ms. The λ_2-criterion, based on the minimum local pressure, is used for the detection of the vortices (Jeong and Hussain 1995). It can be seen (Figs. 8 and 9) that the K-H vortices, which develop in the jet shear layer, separate in transverse large-scale structures in front of the probe P1; the transverse vortices impinge the wall between P1 and P2. The peak in the skin friction coefficient (Fig. 7) corresponds to the

region where the primary structures impinge the wall. It is interesting to note the presence of secondary vortices close to P2 (Fig. 8a) just downstream from the location of the primary structures impact. These vortices are generated due to the effect of the primary vortices on the fluid between the vortex ring and the impinged wall. This results in an ejection of rotating fluid from the wall and consequently affects the downstream evolution of the primary vortex, which also detaches from the wall near the probe P2 (Fig. 8c, d). The sudden decrease in the mean skin friction coefficient downstream from the peak location is mostly due to both the generation of the secondary vortex and the detachment of the vortices just downstream from P2. Similar behavior can be observed for the higher Reynolds number (Fig. 9) with two slight differences. First, despite that the secondary structure is formed at similar radial
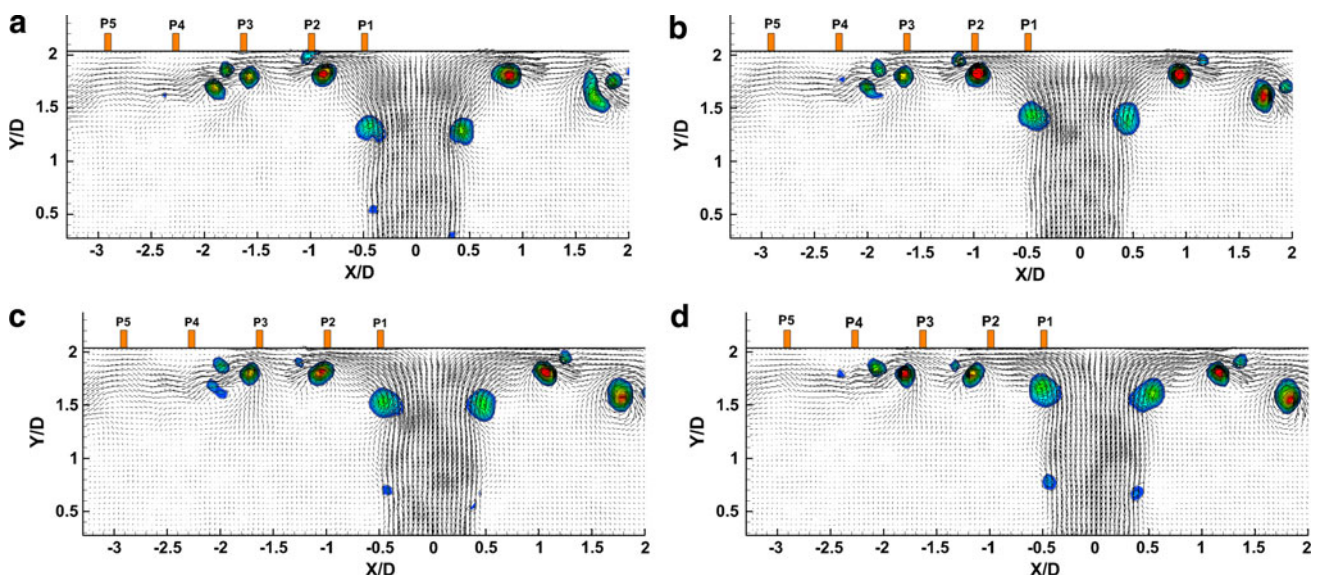

Fig. 8 Vortex dynamics in the impinging region for $Re = 1,260$; the color iso-contours are indicative of the vortex centers
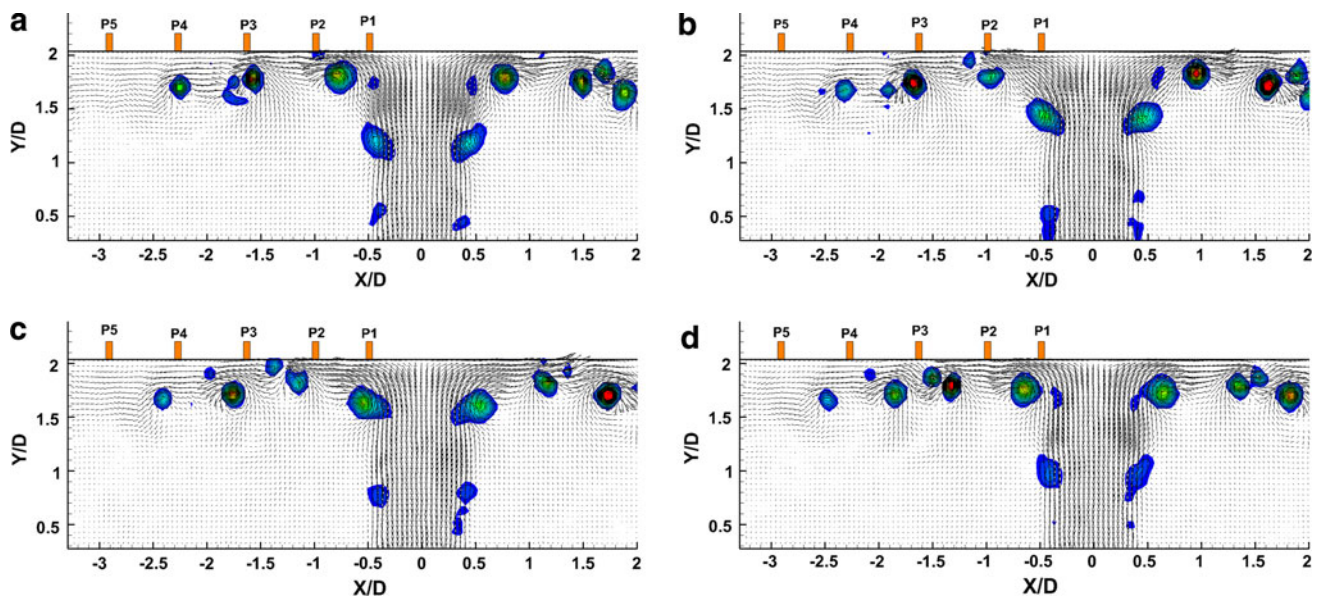
Fig. 9 Vortex dynamics in the impinging region for $Re = 2,450$; the color iso-contours are indicative of the vortex centers

location (close to P2), its detachment occurs further downstream (Fig. 9d) for $Re = 2,450$ when compared to the $Re = 1,260$ case. Second, the detached structures seem to develop closer to the wall near P3 for $Re = 1,260$. The latter phenomenon could explain the slightly slower decrease in the mean skin friction coefficient for $Re = 2,450$ downstream from P3 (cf. Fig. 7). In addition, this vortex dynamics could explain the difference in the skin friction coefficient distribution between the probes P3 and P4.

Landreth and Adrian (1990) used PIV measurements to characterize the velocity field of a circular impinging jet at a Reynolds number of 6564. They evidenced the presence of a secondary vortex at a separation point located below and downstream of the primary vortex, which appears to have lifted away from the boundary layer. Didden and Ho (1985) explained the rise in the magnitude of the fluctuating pressure at the wall-jet region by the formation of secondary vortices. Further downstream, they suggested that the decrease in the pressure fluctuations is due to the ejection or lifting of the secondary vortices. Hall and Ewing (2006) found that the average convection velocity decreased from $U_c = 0.73\ U_0$ in the region between $r/D = 1.0$ and 1.5 to $0.6U_0$ for $r/D = 1.5$ and 2.0. They explained this variation by the separation in this region of the secondary vortices from the wall. In their numerical study, Hadziabdic and Hanjalic (2008) found that strong azimuthal rotation of the toroidal vortices affects the flow in the near-wall region of the impinging circular jet. The formation of a counter-rotating wall-attached bubble with internal recirculation, namely "secondary vortex", was localized between the plate surface and the large-scale toroidal vortex at the wall-jet edge shear layer. The large-eddy simulations of Olsson and Fuchs (1999) of a forced

semiconfined circular impinging jet showed the presence of secondary vortices near the impinged wall only for radial distances higher than 1.19 D from the stagnation point. It was also found that the secondary vortices from downstream of the primary vortices and that the rotation of the secondary vortices affects the flow near the wall by introduction of a wall normal motion and a subsequent lift up.

3.5 Energy spectra and cross-correlations of the wall shear stress

The frequency content of the polarographic signals is obtained from studying the energy spectra at different probes. The most energetic sharp frequency peaks are observed at the probes P1, P2 and P3 for the two studied regimes (Fig. 10a, b). The main peak occurs at a frequency of 13.2 Hz for $Re = 1,260$ and 26.5 Hz for $Re = 2,450$. The higher frequency peaks are harmonics of the main one. Although a low frequency peak can be distinguished at the probes P4 for $Re = 1,260$, a single frequency peak of 26.5 Hz is present at the probe P4 for $Re = 2,450$. This difference is explained by the interaction between the primary and the secondary vortices, which results in lower frequency tertiary structures for $Re = 1,260$. For the higher Reynolds number ($Re = 2,450$), both the tertiary structures and the vortices with higher frequency seem to influence the variation of the wall shear stress.

In this study, the cross-correlation coefficient between two temporal signals $a(t)$ and $b(t)$ is defined by

$$R_{a'b'}(T) = \frac{\overline{a(t)b(t+T)}}{\mathrm{RMS}(a') \times \mathrm{RMS}(b')} \tag{5}$$

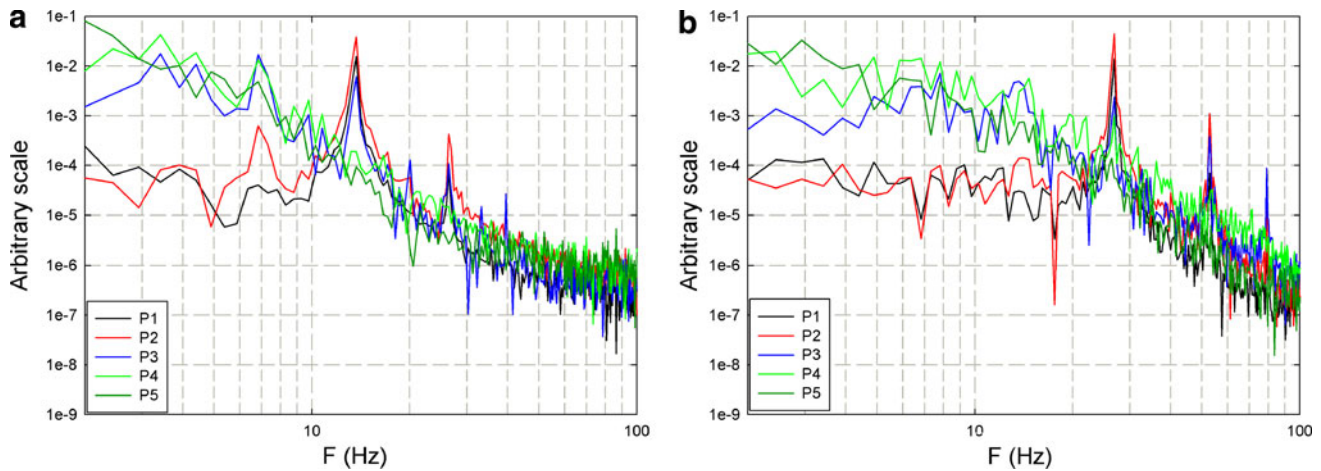where T is the time delay between the signals.

Fig. 10 Energy spectra of the wall shear stress fluctuations for $Re = 1,260$ and 2,450, respectively

Figure 11a, b show the distribution of the cross-correlation coefficient, calculated between different polarographic signals, for $Re = 1,260$ and 2,450, respectively. Most of the correlation plots are periodic with a frequency of about 13.2 Hz for $Re = 1,260$ and about 26.5 Hz for $Re = 2,450$, which corresponds to the transverse vortex passing. This distribution indicates that the transverse large-scale structures are the main features, which affect the wall shear stress. The correlation between P1 and P2 shows strong dependency between the events that affect the wall shear stress at the two probes. The high amplitude of the correlation peak between P1 and P2 suggests that the transverse vortex passing is the main physical phenomenon responsible for the velocity gradient variation at the wall for these probes. On the other hand, the generation of secondary vortices near P2 and the interactions between the

primary and the secondary vortices, when the radial distance increases, could explain the lower cross-correlation amplitude between P1 and P3. Similar phenomena can explain the cross-correlation amplitude between P2 and P3. The low amplitude of the P1–P3 and P2–P3 cross-correlations for $Re = 2,450$ as compared to $Re = 1,260$ is related to stronger interaction between the secondary vortices and the impinged wall, whereas these structures detached just downstream from their generation location for $Re = 1,260$. The global effect of the primary vortices on the flow dynamics at different probes can explain the periodicity of the P1–P4 and P2–P4 correlations, despite their low amplitude. Finally, the advection of bigger structures that result from the interaction between primary and secondary vortices could explain the particular P3–P4 cross-correlation shape.
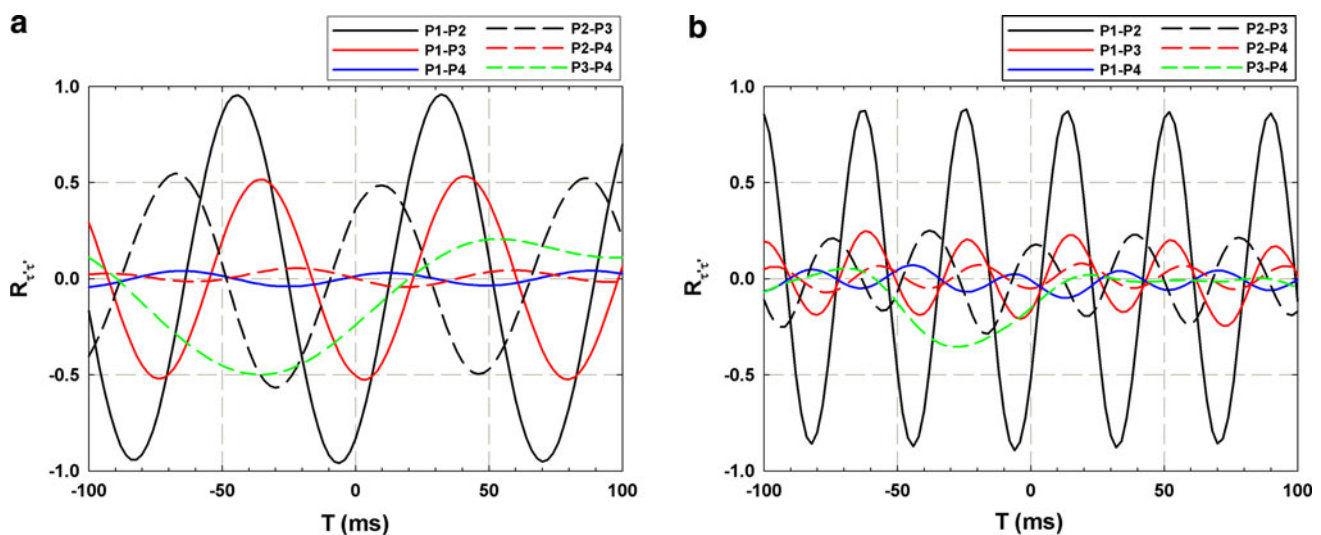

Fig. 11 Cross-correlations between the wall shear stress fluctuations for $Re = 1,260$ and 2,450, respectively

3.6 Wall shear stress dependency on the streamwise velocity and the transverse vorticity

From the above results, it is evident that the wall shear stress is strongly dependent on the large-scale vortical structures dynamics. The cross-correlation coefficients of the wall shear stress with the x-component of the velocity ($R_{\tau'u'}$) and the transverse vorticity ($R_{\tau'\omega_z'}$) are calculated for deeper investigation of the relation between the vortex dynamics and the wall shear stress variations for the two Reynolds numbers. The vorticity signals are extracted from the PIV measurements at different vertical positions from the wall. Figure 12 shows two main differences between the distribution of $R_{\tau'u'}$ and $R_{\tau'\omega_z'}$. First, while both cross-correlations present high amplitude near the wall, a decrease followed by an increase presents near the wall occurs farther from the wall for $R_{\tau'u'}$ as compared to $R_{\tau'\omega_z'}$. Second, $R_{\tau'\omega_z'}$ becomes negligible at around 4 mm from the wall, while $R_{\tau'u'}$ gradually decreases when the vertical position increases and the wall shear stress still correlates the velocity farther from the wall. These differences are related to the influence of the vortex passing on the velocity field near the wall but also far from the wall. The entrainment of the surrounding flow is strongly influenced by the passage of the K-H structures (El Hassan and Meslem 2010; El Hassan et al. 2011). Therefore, the presence of important cross-correlation between the velocity and the wall shear stress far from the wall is due to the influence of the transverse structures on the surrounding fluid where no vortical structures can be detected. Near the wall, a phase jump is observed for both $R_{\tau'u'}$ and $R_{\tau'\omega_z'}$ but its vertical location is different for the two cross-correlation coefficients. This jump, better illustrated in Fig. 13, occurs at a vertical position between 1.7 and 2.1 mm from the wall for $R_{\tau'u'}$ and between 0.1 and 0.4 mm for $R_{\tau'\omega_z'}$. The latter indicates that the wall shear stress highly correlates with

the K-H structures after their separation but also with the secondary vortices. The jump in $R_{\tau'u'}$ indicates the transition from the direct influence of the large-scale transverse vortices on the wall shear stress to an indirect relation between the x-component of the velocity and the wall shear stress due to the influence of the vortices on the surrounding flow.

It can be concluded that the cross-correlation between the wall shear stress and the transverse vorticity is of high interest for studying the relation between the dynamics of the primary and the secondary vortices and the wall shear stress. In the next paragraph, $R_{\tau'\omega_z'}$ is calculated between the vorticity signals and the wall shear stress variations for different polarographic probes.

3.7 Wall shear stress and transverse vorticity cross-correlations

The cross-correlations between the wall shear stress and the transverse vorticity fluctuations are presented at different polarographic probes and the two regimes in Figs. 14 and 15. The periodicity of the cross-correlations and the high amplitude of the correlation coefficient confirm that the wall shear stress is strongly dependent on the dynamics of the large-scale transverse vortical structures. It is shown that near the wall, no time delay exists between the vortical passing and their influence on the wall shear stress for the probe P1. Two regions can be distinguished (near the wall): the zone close to the wall and the primary vortices passing region. The presence of these two regions suggested that although the secondary vortices are not formed at this radial position, a like-ejection effect seems to exist due to the passing of the primary large-scale structures. Therefore, negative value of $R_{\tau'\omega_z'}$ is observed for $T = 0$, and positive values characterize the region where the primary vortices develop. The cross-correlation

Fig. 12 Planar representation of the cross-correlations between the wall shear stress and, respectively, the velocity and the transverse vorticity for $Re = 1,260$ at the probe P2
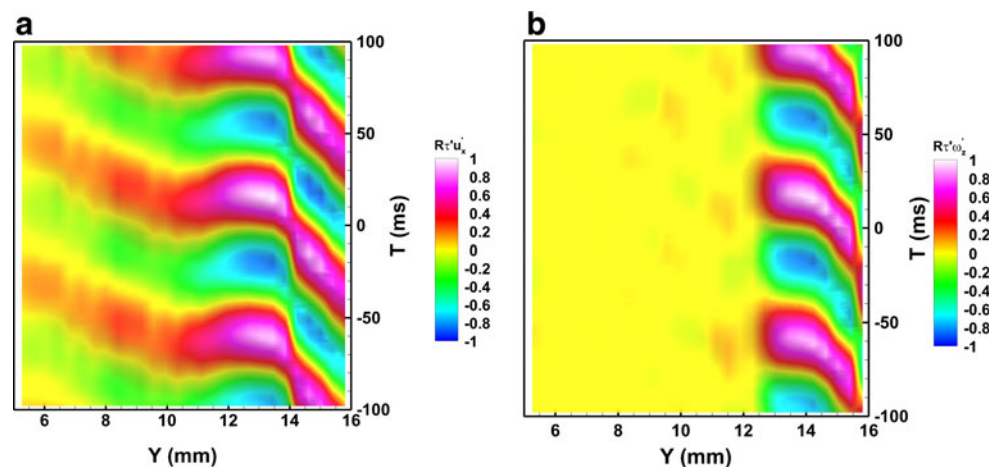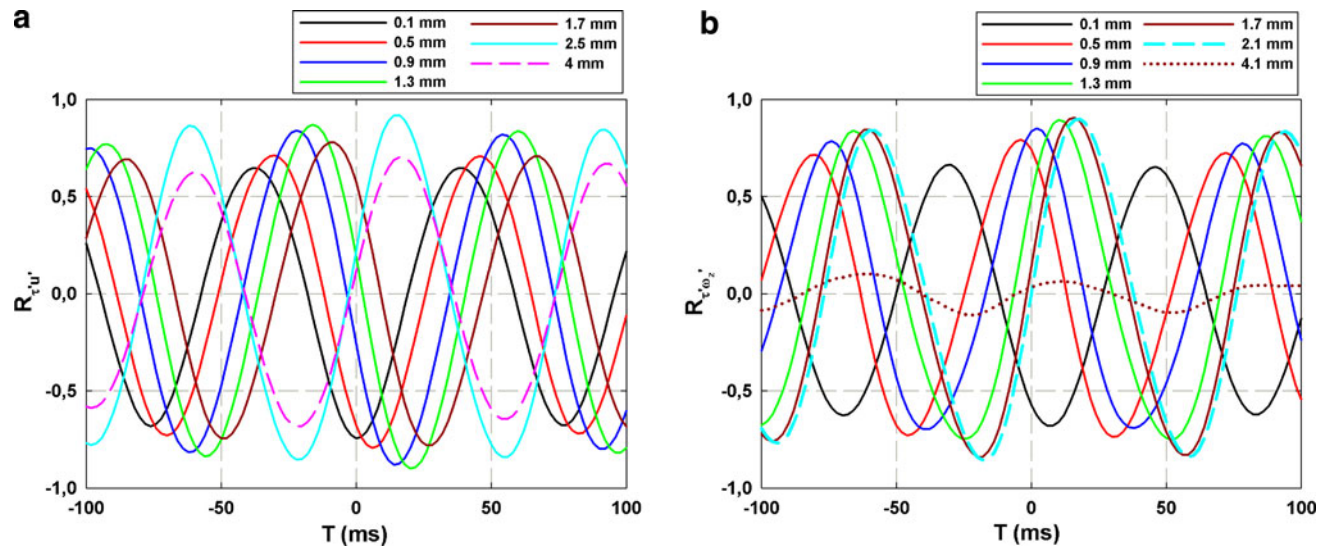
Fig. 13 2D representation of the cross-correlations between the wall shear stress and, respectively, **a** the velocity and **b** the transverse vorticity for $Re = 1,260$ at the probe P2; the origin is taken at the impinging wall (at P2) and different distances from the wall are considered

distributions are quite similar for the two studied Reynolds numbers; the frequency peaks correspond to the transverse vortices passing (13.2 Hz for $Re = 1,260$ and 26.5 Hz for $Re = 2,450$). The same explanation concerning the influence of the vortices passing on the wall shear stress is still valid for P2 (Fig. 14c, d). However, the negative values at $T = 0$ are due to the effect of the secondary vortices, which are generated near P2. For the higher Reynolds number, the cross-correlation values remain higher farther away from the impinged wall as compared to the $Re = 1,260$ case.

For the probe P3, although the cross-correlation shape is different from that at the probes P1 and P2, its periodicity for the two Reynolds numbers (Fig. 14e, f) suggests that the wall shear stress is still strongly dependent on the vortical structures passing. However, the larger period observed for this probe is due to the influence of tertiary structures, which result from the interaction between the primary and the secondary vortices before their detachment near the probe P3.

Figure 15a–d show that the cross-correlation distribution is not periodic for the probes P4 and P5. It is also shown that cross-correlation amplitudes between the wall shear stress and the transverse vorticity are high closer to the wall for the higher Reynolds number. However, the maximum cross-correlation amplitude is higher for the smaller Reynolds number. One can note that the cross-correlation near the wall is negligible for $Re = 1,260$ at P5, whereas high correlation amplitude is present far from the wall. One could suggest that the wall shear stress is influenced by the large-scale vortices even after their detachment far from the impinged wall.

4 Conclusion

The wall shear stress is investigated experimentally using the polarographic method in a circular impinging jet for Reynolds numbers of 1,260 and 2,450. The velocity field and the vortex dynamics are obtained thanks to time-resolved PIV measurements. The simultaneous measurements of the wall shear stress and the velocity field are used to bring out the role of different large-scale vortical structures on the wall shear stress distribution on the impinged wall. The main conclusions of the present study can be summarized as follows.

1. The momentum thickness increases downstream from the jet exit until $X/D = 0.77$ with an expansion rate higher for the lower Reynolds number. Further downstream ($X/D > 1.2$), the momentum thickness becomes almost constant.

2. High turbulence intensity values exist in the free jet and the impinging regions where the azimuthal vortices develop; the maximum turbulence intensity values correspond to the impact region of the transverse structures. The location of the peak in the U_x distribution (between P1 and P2) is different from that of the corresponding turbulence intensity. This spatial distribution is related to the fact that the secondary vortices are generated downstream from the impinging region of the primary structures.

3. The distribution of the mean skin friction coefficient presents a peak in the region where the primary large-scale structures impinge the wall. This maximum is followed by a decrease of the skin friction coefficient, which corresponds to the location of the detachment of the large-scale vortices from the wall.
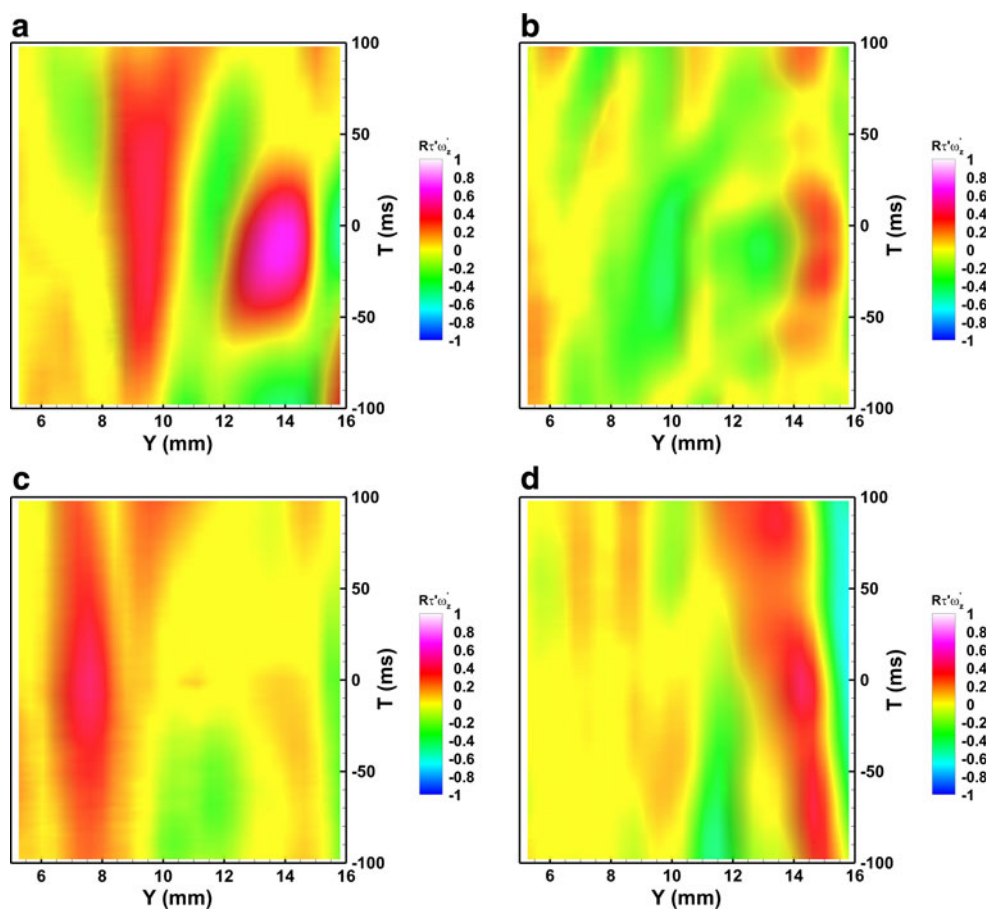
Fig. 14 Cross-correlations between the wall shear stress and the transverse vorticity for different vertical distances from the impinged wall; the *top*, *middle* and *bottom* figures correspond to P1, P2 and P3, respectively; **a, c, e**: $Re = 1,260$; **b,d, f**: $Re = 2,450$
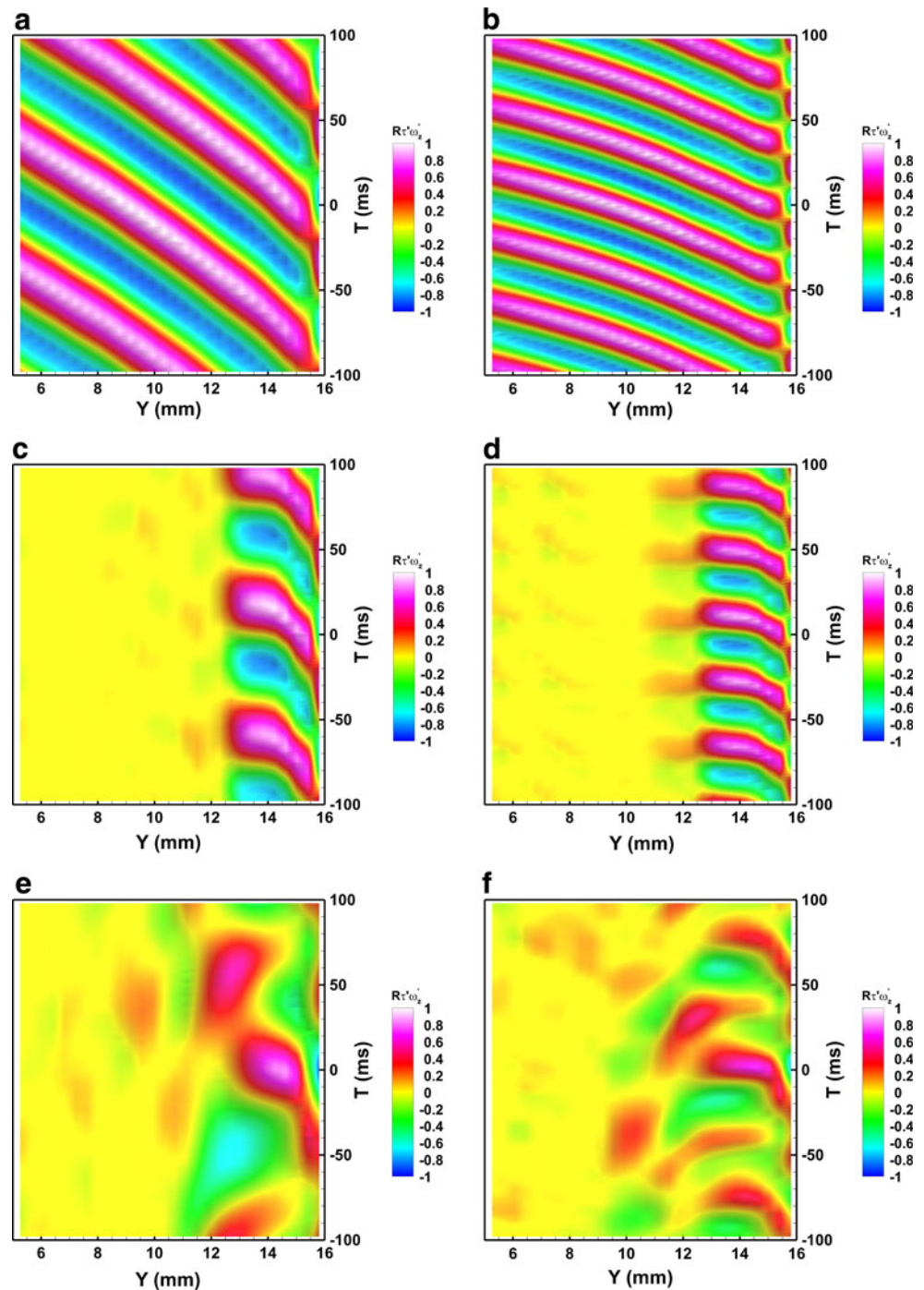
4. The frequency content of the energy spectra of the wall shear stress suggests that vortices with lower frequency (tertiary vortices) influence the variation of the wall shear stress when the radial distance increases. When the Reynolds number increases, both the vortices with high and lower frequencies affect the variation of the wall shear stress.

5. The wall shear stress cross-correlations confirm the important role of different large-scale vortical structures on the wall shear stress distribution. It is found that similar vortex dynamics influences the velocity gradient at the wall for the probes P1 and P2, whereas both the generation of the secondary vortices and the separation of the boundary layer

from the impinged wall affect the wall shear stress for the other probes.

6. Cross-correlations between the wall shear stress and the transverse vorticity fluctuations are used for deeper investigating the role of the vortical structures on the wall shear stress. High cross-correlation amplitudes are observed near the wall where the transverse structures develop. No time delay exists between the primary vortex passing and their influence on the wall shear stress at the probes P1 and P2. Close to the wall, the secondary structures correlate the wall shear stress. Negative cross-correlation values result for $T = 0$ and positive values are present in the region where the primary vortices develop. For P3, tertiary vortices that result from the interaction between primary and secondary structures strongly correlate the wall shear stress. The non-periodicity of the cross-correlation distribution at the probes P4 and P5 is related to the detachment of the vortices upstream from these probes. However, the influence of the large-scale structures is still observed at these probes, particularly near the wall for P4 and far from the wall for P5 at the lower Reynolds number.

References

Alekseenko SV, Markovich DM, Semenov VI (1997) Effect of external disturbances on the impinging jet structure. In: Fourth world conference on experimental heat transfer, fluid mech. and thermodynamics, Brussels, Belgium, June 26, pp 1815–1822

Alekseenko S, Bilsky A, Heinz O, Ilyushin B, Markovich D, Vasechkin V (2002) Fine structure of the impinging turbulent jet. In: Fifth international symposium on engineering turbulence modeling and experiments

Bouainouche M, Bourabaa N, Desmet B (1997) Numerical study of the wall shear stress produced by the impingement of a plane turbulent jet on a plate. Intl J Numer Meth Heat Fluid Flow 7:548–564

Bradshaw P, Love EM (1961) The normal impingement of a circular air jet over a flat surface. ARC R&M 3205

Cerra AW, Smith CR (1983) Experimental observations of vortex ring interaction adjacent to a surface, Report No. FM-4, Department of Mechanical Engineering and Mechanics, Lehigh University, Bethlehem, PA

Clauser FH (1956) The Turbulent boundary layer. Adv Appl Mech 4:1–51

Downs SJ, James EH (1987) Jet impingement heat transfer—a literature survey. ASME Paper no 87-HT-35

Deshpande MD, Vaishnav RN (1982) Submerged laminar jet impingement on a plane. J Fluid Mech 114:213–236

Didden N, Ho C-M (1985) Unsteady separation in a boundary layer produced by an impinging jet. J Fluid Mech 160:235–256

Doligalski TL (1994) Vortex interactions with walls. A Rev Fluid Mec 26:573–616

El Hassan M, Meslem A (2010) Time-resolved stereoscopic PIV investigation of the entrainment in the near field of circular and daisy-shaped orifice jets. Phys Fluids 22:035107

El Hassan M, Meslem A, Abed-Meraim K (2011) Experimental investigation of the flow in the near-field of a cross-shaped orifice jet. Phys Fluids 23:045101

Fabris D, Liepmann D, Marcus D (1996) Quantitative experimental and numerical investigation of a vortex ring impinging on a wall. Phys. Fluids 8:2640

Fourguette D, Modaress D, Taugwalder F, Wilson D, Koochesfahani M, Gharib M (2001) Miniature and MOEMS flows sensors. In: 31st AIAA fluid dynamics conference and exhibition, Anaheim, CA

Gharib M, Modaress D, Fourguette D, Wilson D (2002) Optical microsensors for fluid flow diagnostics. In: 40th AIAA aerospace sciences meeting and exhibition, Reno, NV

Hall JW, Ewing D (2006) On the dynamics of the large-scale structures in round impinging jets. J Fluid Mech 555:439–458

Hadziabdic M, Hanjalic K (2008) vortical structures and heat transfer in a round impinging jet. J Fluid Mech 596:221–260

Harvey JK, Perry FJ (1971) Flow field produced by trailing vortices in the vicinity of the ground. AIAA J 9:1659–1660

Ho C-M, Nosseir NS (1981) Dynamics of an impinging jet. Part 1. The feedback phenomenon. J Fluid Mech 105:119–142

Hrycak P (1981) Heat transfer from impinging jets a literature review. Report AFWAL-TR-81-3054, Flight Dynamics Laboratory, Air Force Wright Aeronautical Laboratories, Air Force System Command, Wright- Patterson AFB, Ohio 45433

Jambunathan K, Lai E, Moss MA, Button BL (1992) A review of heat transfer data for single circular jet impingement. Int J Heat Fluid Flow 13(2):106–115

Janetzke T, Nitsche W (2009) Time resolved investigations on flow field and quasi wall shear stress of an impingement configuration with pulsating jets by means of high speed PIV and a surface hot wire array. Int J Heat Fluid Flow 30:877–885

Jeong J, Hussain F (1995) On the identification of a vortex. J Fluid Mech 285:69–94

Kataoka K, Mizushina T (1974) Local enhancement of the rate of heat-transfer in an impinging round jet by free-stream turbulence. In: Proceedings of 5th international heat transfer conference, Tokyo 305

Kristiawan M, Meslem A, Nastace I, Sobolik V (2012) Wall shear rate and mass transfer in impinging jet. Comparison of circular convergent and cross shaped orifice nozzles. Int J Heat Mass Transf 55:282–293

Landreth CC, Adrian RJ (1990) Impingement of a low Reynolds number turbulent circular jet onto a flat plate at normal incidence. Exp Fluids 9:74–84

Lee J, Lee S-J (2000) The effect of nozzle configuration on stagnation region heat transfer enhancement of axisymmetric jet impingement. Int J Heat Mass Transf 43:3497–3509

Liang S, Falco RE, Bartholomew RW (1983) Vortex ring moving wall interactions: experiments and numerical modelling. Bull Am Phys Soc 28:1397

Looney MK, Walsh JJ (1984) Mean-flow and turbulent characteristics of free and impinging jet flows. J Fluid Mech 147:397–429

Loureiro JBR, Freire APS (2009) Impingement of a confined axisymmetric jet on smooth and rough flat plates: near wall behaviour. Turbul Heat Mass Transf. doi:10.1615/ICHMT

Martin H (1977) Heat and mass transfer between impinging gas jets and solid surfaces. Adv Heat transf 13:1–60

Naguib AM, Koochesfahani MM (2004) On wall-pressure sources associated with the unsteady separation in a vortex-ring wall interaction. Phys Fluids 16(7):2613–2622

Nishino N, Samada M, Kasuya K, Torii K (1996) Turbulence statistics in the stagnation region of an axisymmetric impinging jet flow. Int J Heat Fluid Flow 17:193–201

Olsson M, Fuchs L (1998) Large eddy simulations of a forced semiconfined circular impinging jet. Phys Fluids 10(2):476–486

Orlandi P, Verzicco R (1993) Vortex rings impinging on walls: axisymmetric and three-dimensional simulations. J Fluid Mech 256:615–646

Phares DJ, Holt JK, Smedley GT, Flagan RC (2000a) Method for characterization of adhesion properties of trace explosives in fingerprints and fingerprint simulations. J Forensic Sci 45:762–772

Phares DJ, Smedley GT, Flagan RC (2000b) The wall shear stress produced by the normal impingement of a jet on a flat surface. J Fluid Mech 418:351–375

Popiel CO, Trass O (1991) Visualization of a free and impinging round jet. Expl Thermal Fluid Sci 4:253–264

Poreh M, Tsuei YG, Cermak JE (1967) Investigation of a turbulent radial wall jet. J Appl Mech 34:457–463

Prasad A, Adrian R, Landreth C, Offutt P (1992) Effect of resolution on the speed and accuracy of particle image velocimetry interrogation. Exp Fluids 13:105–116

Rehimi F, Aloui F, Ben Nasrallah S, Doubliez L, Legrand J (2006) Inverse method for electrodiffusional diagnostics of flows. Int J Heat Mass Transf 49:1242–1254

Reiss LP, Hanratty TJ (1962) Measurement of instantaneous rates of mass transfer to a small sink on a wall. AICHE J 8:245–247

Rubel A (1980) Computations of jet impingement on a flat surface. AIAA J 18:168–175

Rubel A (1983) Inviscid axisymmetric jet impingement with recirculating stagnation regions. AIAA J 21:351–357

Sakakibara J, Hishida K, Maeda M (1997) Vortex structure and heat transfer in the stagnation region of an impinging plane jet. Int J Heat Mass Transf 40(13):3163–3176

Sakakibara J, Hishida K, Phillips RC (2001) On the vertical structure in a plane impinging jet. J Fluid Mech 434:273–300

Scholtz MT, Trass O (1970) Mass transfer in a nonuniform impinging jet. AICHE J 16:82–90

Smedley GT, Phares DJ, Flagan RC (1999) Entrainment of fine particles from surfaces by impinging shock waves. Exp Fluids 26(1/2):116–125

Sobolik V, Wein O, Cermak J (1987) Simultaneous measurement of film thickness and wall shear stress in wavy-film flow of non-Newtonian fluids. Collect Czech Chem Commun 52:913

Strand T (1964) On the theory of normal ground impingement of axisymmetric jets in inviscid incompressible flow. AIAA Paper 64–424

Vejrazka J, Tihon J, Marty Ph., Sobolik V (2005) Effect of an external excitation on the flow structure in a circular impinging jet. Phys Fluids 17:105102

Walker JDA, Smith CR, Cerra AW, Doligalski TL (1987) The impact of a vortex ring on a wall. J Fluid Mech 181:99–140

Westerweel J (1993) Digital particle image velocimetry. Delft University Press, Delft

Yapici S, Kuslu S, Ozmentin C, Ersahan H, Pekdemir T (1999) Surface shear stress for a submerged jet impingement using electrochemical technique. J Appl Electrochem 29:185–190

Yokobori S, Kasagi N, Hirata M (1983) Transport phenomena at the stagnation region of a two-dimensional impinging jet. Trans JSME Ser B 49(441):1029–1039

Zhe J, Modi V (2001) Near wall measurements for a turbulent impinging slot jet. J Fluid Eng 123(1):112–120